Deformable registration of X-ray and MRI for post-implant dosimetry in low-dose-rate prostate brachytherapy

William T. Hrinivich[1], Seyoun Park[2], Yi Le[3], Daniel Y. Song[1], Junghoon Lee[1]*

1. Department of Radiation Oncology and Molecular Radiation Sciences, Johns Hopkins University, Baltimore MD, 21287, USA
2. Department of Radiology, Johns Hopkins University, Baltimore MD, 21287, USA
3. Department of Radiation Oncology, Indiana University, Indianapolis, IN, 46202, USA

Version typeset June 17, 2019

*corresponding author
email: junghoon@jhu.edu
address: Department of Radiation Oncology
and Molecular Radiation Sciences
401 N Broadway
Baltimore, MD, 21287

Abstract

Purpose: Dosimetric assessment following permanent prostate brachytherapy (PPB) commonly involves seed localization using CT and prostate delineation using co-registered MRI. However, pelvic CT leads to additional imaging dose and requires significant resources to acquire and process both CT and MRI. In this study, we propose an automatic post-implant dosimetry approach that retains MRI for soft-tissue contouring, but eliminates the need for CT and reduces imaging dose while overcoming the inconsistent appearance of seeds on MRI with three projection X-rays acquired using a mobile C-arm.

Methods: Implanted seeds are reconstructed using X-rays by solving a combinatorial optimization problem and deformably registered to MRI. Candidate seeds are located in MR images using local hypo-intensity identification. X-ray based seeds are registered to these candidate seeds in three steps: 1) rigid registration using a stochastic evolutionary optimizer, 2) affine registration using an iterative closest point optimizer, and 3) deformable registration using a local feature point search and non-rigid coherent point drift. The algorithm was evaluated using 20 PPB patients with X-rays acquired immediately post-implant and T2 weighted MR images acquired the next day at 1.5 T with mean $0.8\times0.8\times3.0$ mm^3 voxel dimensions. Target registration error (TRE) was computed based on the distance from algorithm results to manually identified seed locations using co-registered CT acquired the same day as the MRI. Dosimetric accuracy was determined by comparing prostate D90 determined using the algorithm and the ground truth CT-based seed locations.

Results: The mean±standard deviation TREs across 20 patients including 1774 seeds were 2.23 ± 0.52 mm (rigid), 1.99 ± 0.49 mm (rigid+affine), and 1.76 ± 0.43 mm (rigid+affine+deformable). The corresponding mean±standard deviation D90 errors were 5.8±4.8%, 3.4±3.4%, and 2.3±1.9%, respectively. The mean computation time of the registration algorithm was 6.1 s.

Conclusion: The registration algorithm accuracy and computation time are sufficient for clinical PPB post-implant dosimetry.

ii

Contents

iii

I.   Introduction

Permanent prostate brachytherapy (PPB) is a standard treatment option for localized prostate cancer[1] and favorable results from recent clinical trials suggest that PPB utilization will increase.[2,3,4] Safe delivery of a therapeutic dose using PPB depends critically on the final implanted seed locations, which must be localized in the imaging coordinate system for dose calculation and evaluation of dose delivered to the prostate and nearby organs at risk (OARs). During the implant, seed locations are typically verified using transrectal ultrasound (TRUS) due to its non-invasive real-time imaging capabilities.[5] However, seeds can be difficult to localize using TRUS due to artifacts caused by tissue interfaces and the seeds themselves. Furthermore, intra-operative dose metrics are impacted by edema caused by the implant, which dissipates over time as the dose is deposited.[6] For these reasons, a post-implant dosimetric assessment is considered mandatory, involving the localization of seeds, prostate boundaries, and organs at risk between 0 and 42 days after the implant.[7,8,9]

Post-implant dosimetry is conventionally performed using CT due to its widespread availability and high contrast produced by metallic seeds.[7] However, soft tissue contrast in CT is limited, leading to prostate contouring uncertainty, which propagates to uncertainty in the final dose metrics.[10] To overcome this limitation, a multi-modality approach has been recommended taking advantage of the unparalleled soft tissue contrast of MRI.[11] This approach makes use of co-registered CT and MRI to localize the seeds and organs, respectively. This approach has demonstrated reduced dosimetric variability compared to CT-only post-implant dosimetry[11,12] and has been adopted by many clinics.

While the combined MRI and CT approach improves dosimetric accuracy compared to a CT-only approach, it is resource intensive and still subject to limitations. The approach requires transporting the patient between the MRI and CT suites, creating the potential for prostate deformations due to changes in position, bladder and rectum filling. CT slice thickness on the order of 1-3 mm limits seed localization accuracy,[12] and registration between CT and MRI may be subject to errors. Advanced MRI-to-CT registration techniques have been developed to mitigate error;[13] however, workflows eliminating the need for both CT and MRI are desirable to reduce resource requirements, reduce imaging dose, limit motion, and improve accuracy further.

Last edited $June 17, 2019$

Two primary techniques have been proposed to overcome limitations of current MRI and CT-based dosimetry. The first is MRI-based seed localization. Metallic seeds do not generate signal intensity using conventional pulse sequences, so appear as signal voids leading to some non-seed features identified as seeds (false positives) and some missing seeds (false negatives).[14,15] Seeds designed to generate positive contrast have been demonstrated, but are not typically integrated with isotopes used for therapy.[16] Balanced steady-state free precession (bSSFP) pulse sequences can improve MRI quality for seed identification[17] and susceptibility-based pulse sequences have been developed to provide positive contrast with conventional seeds.[18,19] Susceptibility-based pulse sequences have recently been combined with machine learning-based automatic seed localization enabling all implanted seeds to be localized within 0.7 mm error in phantoms.[20] Preliminary evidence suggests that this performance may translate to patients;[21] however, to the authors' knowledge, robust MRI-only seed localization has not been validated in patients and may require hardware and software upgrades for implementation in many clinics. The second technique involves the combination of projection X-rays and MRI for seed localization acquired sequentially using a custom imaging facility (XMR).[22,23] By mechanically linking the X-ray and MRI systems, the images are inherently registered enabling reliable seed and soft tissue localization. However, this system is not widely available, limiting its utility for most clinics.

Our group has previously developed a multi-modality imaging approach for intra-operative PPB dosimetry combining X-ray projection images and TRUS,[24,25] taking advantage of reliable seed localization using X-rays similar to the XMR system. However, our automatic seed reconstruction algorithm is unique in its ability to use a limited set of images acquired using a commonly available mobile C-arm while providing improved seed reconstruction accuracy relative to CT, with errors ≤ 0.5 mm.[24,26] A similar approach combining X-rays and MRI is desirable for post-implant dosimetry, which would eliminate the need for CT, thereby decreasing radiation dose from imaging and improving seed localization accuracy without requiring specialized hardware. Specifically, this approach would involve X-ray imaging for seed reconstruction followed by MR imaging for prostate and OAR contouring, and registration of the two modalities for post-implant dose calculation and plan evaluation in the MRI coordinate system. However, unlike intra-operative TRUS, X-rays and MRI cannot be acquired without moving the patient, even if the distance is small when using a mobile C-arm, creating the potential for local deformations which our previous intra-operative

I.   INTRODUCTION

[133] algorithm did not account for.[25]

[134]   Multiple rigid, affine, and non-rigid algorithms have been proposed for three-dimensional [135] point set registration in the presence of noise and missing data, as reviewed by Tam et al.[27] [136] Deformable registration techniques include minimizing the mean squared distance between [137] the moving and fixed point sets using gradient descent optimization while regularizing the [138] point translations using a deformation model such as a thin-plate spline.[28] Coherent point [139] drift (CPD) is an iterative non-rigid registration technique in which the moving point set is [140] represented as a Gaussian mixture model (GMM), and the fixed point set is represented as [141] observations of the model.[29] The centroids of the GMM are updated using an expectation [142] maximization approach, and translations are regularized to maintain point topology using [143] motion coherence theory.[30] CPD may be less subject to local minima than gradient descent-[144] based registration, but still may result in sub-optimal solutions in the presence of large initial [145] translations or rotations.[31] Robust rigid initialization has been proposed using stochastic [146] methods such as random sample consensus (RANSAC) or 4-points congruent sets (4PCS).[32] [147] Combining these approaches may provide robust deformable registration of X-ray and MRI [148] as required clinically.

[149]   In this study, we propose a deformable registration approach to align X-ray-based seeds [150] and MRI using non-rigid CPD and initialized using stochastic minimization of mean squared [151] distances between X-ray-based seeds and MRI-based candidate seeds. This algorithm is ini-[152] tialized using an existing X-ray-based seed reconstruction approach.[24,33] Our group previ-[153] ously presented a preliminary gradient descent-based deformable X-ray to MRI registration [154] algorithm for post-implant dosimetry that was evaluated in a subset of implanted seeds.[34] [155] To our knowledge, this is the only existing intensity-based registration method evaluated [156] for this purpose. In the present study, CPD registration algorithm accuracy is evaluated [157] in terms of target registration error (TRE) and dosimetry by comparing all implanted seed [158] locations and resultant dose distributions with those determined using the standard MRI [159] and CT approach. We also analyze the impact of variations in candidate seed localization on [160] algorithm accuracy, propose optimal candidate seed localization parameters, and compare [161] the CPD registration approach to the previous gradient descent-based approach.[34]

Last edited $June 17, 2019$

II. Methods

II.A. Image Acquisition

Twenty prostate cancer patients treated with TRUS-guided PPB using Theragenics model 200 ^{103}Pd seeds (Theragenics Corp., Buford GA) at Johns Hopkins Hospital were included in this study, including 1777 implanted seeds. Three X-rays were taken immediately following seed implantation using an OEC 9800 mobile C-arm (GE Healthcare, Chicago IL) as part of an IRB-approved protocol for intra-operative dosimetry, and were acquired within a 20° angle around the anterior-posterior axis between the patient's legs, e.g. approximately -10°, 0° (anterior-posterior), and 10°. Resultant X-ray images had pixel dimensions of 0.4×0.4 mm^2. MRI and CT scans were performed one day after seed implantation for routine clinical post-implant dosimetry using a 1.5 T Magnetom Espree MRI scanner (Siemens Medical Systems, Erlangen, Germany) and Brilliance Big Bore CT scanner (Philips, Andover MA). MR images were acquired with a body coil (no endorectal coil was used) using a two-dimensional T2 weighted spin echo pulse sequence with 8690 ms repitition time (TR), 104 ms echo time (TE), and 150° degree flip angle. Resultant images had 3 mm slice thickness and mean (range) in-plane voxel dimensions of 0.8 (0.5-1.3) mm. CT images had mean (range) slice thicknesses of 3.0 (2.9-4.0) mm and in-plane voxel dimensions of 0.5 (0.4-0.6) mm. A physician contoured the prostate on all MR images.

We identified twenty clinical cases with MRI and CT that could be aligned well rigidly, making the cases well-suited for registration algorithm validation. Note that in the data sets used for algorithm validation in this study, X-rays were acquired immediately following implantation while MRI and CT were acquired the next day as required clinically. In this workflow, seed migration may occur, and the patient position is changed from lithotomy for X-ray to supine for MRI and CT. Therefore, the images used in this study represent more challenging registration problem than the expected clinical scenario where X-ray and MRI scans will take place on the same day.

II.B. Registration Algorithm

Fig. 1 provides a flow chart outlining major steps of the algorithm, indicating the two deformable registration methods investigated in this study. Implanted seeds are reconstructed

II. METHODS

¹⁹¹ from three X-rays by solving a combinatorial optimization problem[24,33] and registered to MR
¹⁹² images using an intensity-based points-to-volume registration method. As a pre-processing
¹⁹³ step, MR images are filtered to identify candidate seed locations, which are converted to
¹⁹⁴ a smooth distance map. The X-ray-based seed locations are then rigidly registered to the
¹⁹⁵ distance map using a stochastic evolutionary optimizer.[35] The rigid registration is refined
¹⁹⁶ using an iterative closest point (ICP) algorithm that estimates an optimal affine transfor-
¹⁹⁷ mation using singular value decomposition (SVD) at each iteration.[36,37] The results of the
¹⁹⁸ affine registration are used to refine the candidate seed locations and distance map. While
¹⁹⁹ the ICP algorithm can also be implemented for rigid registration, the iterative approach is
²⁰⁰ highly susceptible to local minima. For this reason, we chose to initialize the algorithm using
²⁰¹ the stochastic optimizer, thereby improving algorithm robustness to changes in pose.

²⁰²   Finally, a deformable registration step is used to account for local tissue deformations
²⁰³ and seed migration. We compare two deformable registration methods 1) an iterative non-
²⁰⁴ rigid CPD algorithm regularized using motion coherence theory[29] and 2) gradient descent
²⁰⁵ optimization of seed translations regularized by imposing forces between adjacent seeds based
²⁰⁶ on a spring model.[34] The output of these algorithms is a set of seed locations in the MRI
²⁰⁷ coordinate system enabling computation of the radiation dose delivered to the prostate and
²⁰⁸ nearby organs at risk.[38,39] The details of each algorithm step are described as follows.

II.B.1.   Seed reconstruction from X-rays

²¹⁰ Seeds are reconstructed from X-rays using an algorithm previously developed by our group.
²¹¹ APC-REDMAPS (REduced-Dimensionality Matching Algorithm for Prostate Seed recon-
²¹² struction with Automatic Pose Correction) simultaneously corrects X-ray image pose errors
²¹³ and reconstructs seeds as a three-dimensional point cloud,[24,33] and is briefly described as
²¹⁴ follows. Three X-ray images are taken at different angles (poses) using an imaging system
²¹⁵ such as a mobile C-arm or kilo-voltage imaging system commonly available on linear accel-
²¹⁶ erators. Image poses are tracked using an X-ray tracking fiducial that consists of a set of
²¹⁷ radio-opaque beads. The seeds and the fiducials are automatically segmented, discriminated
²¹⁸ from one another, and used to detect image pose.[24,40] The three-dimensional seed cloud is
²¹⁹ then reconstructed by determining the unique correspondences of all the seeds among the
²²⁰ images in the presence of partial seed occlusion using binary combinatorial optimization.[33]

II.B.2. MRI Pre-Processing

Permanent brachytherapy seeds do not generate MR signal and typically appear as dark voids in T2 weighted MR images as shown in Fig. 1.[41] We implemented pre-processing steps to identify candidate seed locations using MRI based on local hypo-intensities. First, the MRI was resampled using linear interpolation to have isotropic $0.8{\times}0.8{\times}0.8$ mm^3 voxels to minimize directional bias in the algorithm. Next, background intensity variations in the MRI were mitigated using a filter described by

$$I'_{i,j,k} = (I * K)_{i,j,k} - I_{i,j,k} \tag{1}$$

where $I'_{i,j,k}$ is a filtered image voxel, $I_{i,j,k}$ is a raw image voxel, $*$ represents a two-dimensional convolution, and K is a uniform two-dimensional circular kernel with 5 mm radius oriented in the axial plane. Due to the 3 mm slice thickness, convolution in the out-of-plane direction was not found to influence results so was omitted to decrease computation time. This operation produced the filtered image in Fig. 1, in which candidate seed locations appeared as hyper-intensities.

Candidate seed locations were isolated from the filtered image using a local peak identification algorithm, which exhaustively searched the spherical neighborhood around each voxel within the prostate contour to find the local maximum intensity. The radius of this neighborhood was set as 4 mm. The resultant candidate seeds were sorted in descending order based on the associated filtered image signal intensity. Candidate seeds were retained with filtered image intensity $\geq 10\%$ of the maximum, including a maximum of $1.3N$ candidate seeds where N is equal to the number of seeds in the X-ray based seed cloud. Since the MRI pre-processing step identifies all local hypo-intensities, including some non-seed features such as needle tracks, the threshold of $1.3N$ provided a sufficient number of true positive candidate seed locations for robust registration. This threshold selection is described further in Section II.C.3.

The final set of candidate seeds was then converted to a Danielsson distance map with

---

II. METHODS   II.B. Registration Algorithm

247   isotropic $0.5 \times 0.5 \times 0.5$ mm^3 voxel dimensions.[42] The distance map can be described using

248
$$D(\vec{p}) = \min_{n} \|\vec{p} - \vec{c}_n\| \qquad (2)$$

249   where $D(\vec{p})$ is the value of the distance map at a voxel location $\vec{p}$, and $\vec{c}_n$ is the coordinates

250   of an MRI-based candidate seed.

II.B.3. Rigid Registration

252   The X-ray based seed cloud was initially registered to the distance map by finding the rigid

253   transformation that minimized the mean squared distance between the X-ray-based seeds

254   and the MRI-based candidate seed locations using

255
$$\hat{R} = \arg\min_{R} \frac{1}{N} \sum_{i=1}^{N} D(R\vec{s}_i)^2 \qquad (3)$$

256   where R is a rigid transformation matrix, and $\vec{s}_i$ is the coordinates of a seed in the X-ray based

257   seed cloud containing a total of N seeds. The six degree-of-freedom rigid transformation

258   R was parameterized for optimization using three Euler angles and a three-dimensional

259   translation vector. Equation 3 was minimized using a stochastic evolutionary optimizer.[35]

260   The transformation parameters were initialized assuming zero rotation and a translation

261   vector that aligned the centers of mass of the X-ray-based seeds and the MRI-based candidate

262   seeds. The optimization search space was initialized using parameter scale factors of 10

263   radians^{-1} (0.17 degrees^{-1}) and 1 mm^{-1}, initial search radius of 3 mm, growth factor of 1.1,

264   shrink factor of 0.96, and stopping criterion of the Frobenius norm of the covariance matrix

265   $< 1 \times 10^{-9}$.[35]

II.B.4. Affine Registration

267   To account for potential changes in scale, an affine registration was performed following the

268   rigid registration. We employed an affine ICP algorithm[36] for this purpose with stringent

269   criteria for point correspondences (distance <3 mm) to mitigate the impact of false positive

270   seeds.[25] The ICP algorithm estimates the affine transformation mapping the X-ray-based

271   seeds to the candidate seed locations using the method described by Umeyama,[37] which

---

Last edited $June 17, 2019$ II.B.   Registration Algorithm

uses SVD of the covariance matrix of point positions to estimate a seven degree-of-freedom affine transformation incorporating rotation, translation, and isotropic scaling while avoiding reflections. Point correspondences are estimated at each iteration using a Kd-tree search constrained to a 3 mm radius.[43] The stopping criterion was defined as the change in mean squared residuals $< 1 \times 10^{-8}$ between iterations.

II.B.5. Candidate Seed Location Refinement

The candidate seed locations were refined using the affine registration results by exhaustively searching the spherical neighborhood of each registered seed location for the local maximum in filtered signal intensity. A spherical neighborhood radius of 3 mm was used to identify seeds locally, while mitigating the possibility of identifying an incorrect adjacent seed. This search radius selection is discussed further in Section II.C.3. Refined candidate seed locations were again retained if the associated signal intensity was $\geq 10\%$ of the maximum filtered image intensity.

II.B.6. Deformable Registration

In this study, we investigate the use of two deformable registration techniques to account for local tissue deformation between the X-ray and MRI acquisitions. The two techniques are a CPD approach, optimized using iterative expectation maximization, and a spring-model approach, optimized using gradient descent. Both approaches use the results of the affine registration as the moving point set, and the refined candidate seed locations as the fixed point set. Both approaches also find a transformation function ν that minimizes the distance between the moving point set and the fixed point set using an external energy term $U_E(\nu)$ while maintaining point cloud topology and deformation smoothness using an internal energy (regularization) term $U_I(\nu)$. The general deformable registration cost function is

$$f(\nu) = U_E(\nu) + \frac{\lambda}{2} U_I(\nu) \tag{4}$$

where λ defines the trade-off between goodness of fit and regularization.

II.   METHODS   II.B.   Registration Algorithm

297 **Coherent Point Drift (CPD):**   Non-rigid CPD involves a maximum likelihood estimation
298 of GMM centroid locations (moving point set) translated by a displacement function ν_{CPD}
299 relative to a set of GMM observations (fixed point set). The displacement function ν_{CPD} is
300 a set of weights of Gaussian basis functions defining translations in each direction for each
301 seed in the moving point set. The external energy term is a negative log-likelihood function

$$U_E(\nu_{CPD}) = -\sum_{i=1}^{M} \log \left[\omega \frac{1}{M} + (1-\omega) \sum_{j=1}^{N} \frac{1}{N} p(\vec{c}_i | j, \nu_{CPD}) \right] \tag{5}$$

303 where ω defines the weight of a uniform distribution term corresponding to the expected
304 fraction of outliers in the fixed point set. N and M are the numbers of seeds in the moving
305 and fixed point sets, respectively. The term $p(\vec{c}_i | j, \nu_{CPD})$ is a normalized Gaussian function
306 of the Euclidean distance between the fixed point $\vec{c}_i$ and the transformed moving point
307 $T(\vec{s}_j, \nu_{CPD})$.   The internal energy term represents a high-pass filter of the displacement
308 function

$$U_I(\nu_{CPD}) = \int_{\Re^3} \frac{|\tilde{\nu}(k)|}{\tilde{G}(k,\beta)} dk \tag{6}$$

310 where $G(k, \beta)$ is a Gaussian function with variance β, $\sim$ represents the Fourier transform,
311 and k is the spatial frequency parameter. This regularization enforces motion coherence
312 by limiting high frequency displacement components, causing nearby points have similar
313 displacements as described by motion coherence theory.[29,30] The external and internal energy
314 terms were combined according to Eq. 4. In this study, ω was set to 0.05. β and λ were set
315 to 3, which have been shown to result in robust non-rigid registration results.[29] This cost
316 function was minimized using an iterative expectation maximization approach with stopping
317 criterion of covariance of the GMM $< 1 \times 10^{-5}$. Further details regarding the formulation
318 of the expectation and maximization steps are provided by Myronenko and Song.[29]

319 **Spring Model:**   A gradient-descent based optimization approach regularized using a spring
320 model was employed, extended from the method proposed by Park et al.,[34] which was
321 previously validated on a subset of implanted seeds. Briefly, the refined candidate seed
322 locations were converted to a Danielsson distance map[42], which was truncated at 3 mm to
323 mitigate the influence of distant candidate seeds. This distance map was used to define an

external energy term $U_E(\nu_{spring})$, where ν_{spring} is a set of translation components for each seed in the moving point set. An internal energy term $U_I(\nu_{spring})$ was defined based on a spring model, penalizing changes in distance between nearby groups of seeds. The external and internal energy terms were combined according to Eq. 4 with a λ value of 40. The cost function was minimized using a limited memory bounded quasi-newton BFGS optimizer.[44] The seed translation components were bounded within [-3, 3] mm and optimizer stopping criterion of change in cost function value $< 1 \times 10^{-9}$ between iterations. Further details of the non-linear spring model and derivation of the cost function are provided in the Appendix.

II.C.   Algorithm Validation

The registration algorithm was implemented in C++ using the Insight Segmentation and Registration Toolkit (ITK) (Kitware, Clifton Park NY), Point Cloud Library (PCL),[45] and the CPD library developed by Gadomski (http://www.gadom.ski/cpd) and run on a laptop PC with a 2.6 GHz dual core Intel Core i5-7300U CPU and 16 GB of memory.

II.C.1.   Target Registration Error

Target registration errors (TREs) were calculated following each major step of the registration algorithm to demonstrate and compare the improvements in accuracy attributed to affine and deformable registration methods. Manual CT/MRI-based seed locations were used as the ground truth for TRE calculation. We selected twenty patient data sets for which the CT and MR images exhibited little deformation leading to an accurate rigid registration, and CT seeds were automatically segmented using Variseed treatment planning software (Varian Medical Systems, Palo Alto CA) followed by an expert medical physicist's manual adjustment on the CT image. The CT was rigidly registered to the MRI using a manual landmark approach, where seeds appearing in both images were used as fiducials to align the images. This approach was intended to minimize the registration error of the CT-based seed cloud to the MRI.

TREs were calculated for each seed following each registration method using one-to-one correspondences between the registered X-ray-based seeds and ground truth seeds. A single set of X-ray to ground truth correspondences was determined for each patient using the results of the deformable spring-model registration. This set of correspondences was used to

---

II.   METHODS   II.C.   Algorithm Validation

calculate the TREs for each registration approach, and was determined using an iterative correspondence estimation algorithm in PCL, CorrespondenceEstimationBackProjection.[45] TREs were then calculated as the three-dimensional Euclidean distances between the ground truth and X-ray-based seed locations following each registration method.

The mean, standard deviation (SD), and maximum TRE were calculated for each step of the registration algorithm for each patient. Due to the difference between the axial (in-plane) and superior-inferior (out-of-plane) spatial resolution of the MRI and CT, statistics were also calculated in terms of the in-plane and out-of-plane TRE components. Mean and maximum TREs were compared between the two deformable registration approaches in R using paired t-tests.

II.C.2.   Dosimetric Analysis

Dose distributions were calculated following each registration approach using the TG-43 formalism and Theragenics model 200 ^{103}Pd point source parameters.[38] The clinical source strengths were used to calculate dose distributions for each patient in the MRI coordinate system with isotropic 2 mm dose grids. The post-implant dose distribution calculated based on the clinical CT and MRI registration approach and was used as the ground truth for comparison. The metric of interest was the minimum dose delivered to 90% of the prostate (D90),[8] which was calculated for each patient based on the clinical prostate contour using SlicerRT.[46] The error in prostate D90 was calculated for each patient and registration approach.

II.C.3.   Sensitivity Analysis

Simulations were performed to assess the sensitivity of the rigid and deformable registration results to variations in the hyper-parameters used to identify the candidate seed locations. Since multiple factors may cause MR image quality to vary, robustness to variations in candidate seed identification is important for clinical applicability. Hyper-parameters were systematically varied and the algorithm was re-applied to all 20 patients. TREs were re-computed as described in Section II.C.1. In all simulations, the X-ray-to-ground truth seed correspondences were kept constant based on the deformable registration results obtained in Section II.C.1. to mitigate the impact of seed correspondences on the sensitivity analysis

results.

Rigid Registration: Two parameters impacting the initial candidate seed localization method used for rigid registration are 1) the search radius of the local peak identification step and 2) the constraint on the maximum number of candidate seeds as described in Section II.B.2. The search radius of the local peak identification step was varied from 2 mm to 5 mm in 1 mm increments, and the constraint on the maximum number of candidate seeds was varied from $0.5N$ to $2N$ in $0.1N$ increments, where N is the number of seeds implanted. We investigated the impact of these two parameters on the number of candidate seeds actually identified, and on the resultant mean TRE following rigid registration.

Deformable Registration: The parameter impacting the refined candidate seed localization method used for deformable registration is the local search radius described in Section II.B.5., applied following affine registration. This local search radius was varied from 1 mm to 6 mm in 1 mm increments. The resultant mean and maximum TREs were calculated following deformable registration using the CPD and spring model approaches for each local search radius value.

III.   Results

III.A.   Target Registration Error

Of the 1777 seeds implanted, one seed unidentified on CT for one patient due to potential migration, and two seeds identified >1 cm outside of the prostate in a second patient were excluded resulting in 1774 seeds for validation. Fig. 2 shows example MR images from two patients with seed locations identified at each step of the registration algorithm. The final column contains corresponding images from co-registered CT with manually identified seed locations that were used as the ground truth in this study. Seeds located within 3 mm of the selected slice were displayed in each image, leading to some seeds appearing or disappearing between images.

Fig. 3 contains histograms of TREs of all 1774 seeds following each component of the registration algorithm, showing incremental reductions in TRE with each step. Table 1

III.   RESULTS

₄₀₉ summarizes statistics of total TREs for all 1774 seeds, along with the in-plane (axial) and
₄₁₀ out-of-plane (superior-inferior) TRE components. The patient-specific mean TREs (mean
₄₁₁ $\pm$ SD) for the deformable-spring and deformable-CPD approaches were 1.81 ± 0.48 mm and
₄₁₂ 1.76 ± 0.43 mm, respectively ($p = 0.21$), and patient-specific maximum TREs were 5.37 ± 1.25
₄₁₃ mm and 5.07 ± 1.38 mm, respectively ($p = 0.009$). The in-plane TRE component was larger
₄₁₄ than the out-of-plane component following the rigid and affine registrations, but was smaller
₄₁₅ than the out-of-plane component following deformable registration.

₄₁₆ Fig. 4 contains boxplots of TREs for each individual patient following each step of the
₄₁₇ registration algorithm. In general, TREs decreased with each step of the algorithm for each
₄₁₈ patient. The affine and deformable registration led to incremental improvements in accuracy
₄₁₉ for each individual patient. Specifically, patients with the largest TREs following the rigid
₄₂₀ registration tended to have the largest TREs following affine and deformable registration as
₄₂₁ well. The deformable-CPD approach led to smaller mean TREs than the deformable-spring
₄₂₂ approach in 13 patients and smaller maximum TREs in 15 patients.

₄₂₃ For the CPD approach, 1225 (69.0%), 1599 (90.1%), and 1751 (98.7%) of seeds had
₄₂₄ TREs within 2 mm, 3 mm, and 5 mm, respectively. Visual inspection of the 23 (1.3%)
₄₂₅ seeds with TREs >5 mm showed that 7 were outside of the prostate boundary, 4 were in
₄₂₆ the seminal vesicles, 3 were in the apex, and 1 was in the base. The remaining 8 cases
₄₂₇ appeared to be the result of sub-optimal one-to-one correspondences with the CT-based
₄₂₈ seeds used for TRE calculation. These seeds appeared near groups of other seeds, leading to
₄₂₉ unclear one-to-one correspondences with the CT-based seeds with at least one X-ray-based
₄₃₀ seed assigned to a distant CT-based seed. Since deformations near the prostate periphery
₄₃₁ appeared to contribute to these sub-optimal correspondences, the resultant TREs were not
₄₃₂ excluded from analysis.

₄₃₃ The mean computation times of the APC-REDMAPS X-ray seed reconstruction (includ-
₄₃₄ ing X-ray image segmentation, image pose computation, and seed reconstruction) was 30 s.[26]
₄₃₅ The mean computation times of the deformable-spring and deformable-CPD X-ray to MRI
₄₃₆ registration algorithms (including rigid and affine steps) were 9.6 s and 6.1 s, respectively.

III.B.   Dosimetric Analysis

Example MRI and dose distributions calculated using each registration approach are shown in Fig. 5, along with the ground truth dose distributions derived from the clinical CT-to-MRI registration approach in Fig. 5c). Qualitatively, the dose distribution calculated based on the CPD approach appeared similar to the CT-based dose distribution, particularly near the urethra. Boxplots of the prostate D90 error for each registration approach are shown in Fig. 5a). The mean±SD magnitude of error for the rigid, affine, spring, and CPD approaches was 5.8±4.8%, 3.4±3.4%, 2.7±2.8%, and 2.3±1.9%, respectively. With the CPD approach, 18 (90%) of the patients had prostate D90 error within 5%, and the largest error was -6.8%.

III.C.   Sensitivity Analysis

III.C.1.   Rigid Registration

Plots of the number of candidate seeds identified versus the constraint on the maximum number of candidate seeds are shown in Fig. 6a). Increases in the constraint led to proportional increases in the number of candidate seeds identified up to a plateau value, beyond which the number of candidate seed locations identified remained approximately constant. This plateau value depended on the local peak search radius, where larger radii had lower plateau values. For a 4 mm search radius, the plateau value was approximately 1.25. Corresponding plots of the mean rigid TRE versus the constraint on the maximum number of candidate seeds is shown in Fig. 6b). Mean TREs tended to decrease with increasing constraint value up to a constraint of 1.0, beyond which the mean TRE change depended on the local peak search radius. The 4 mm search radius resulted in low and stable TREs for constraint values between 1.1 and 1.6. A local peak search radius of 4 mm and a constraint on the maximum number of candidate seeds of $1.3N$ were selected as default values.

III.C.2.   Deformable Registration

Plots of the mean and maximum deformable TREs versus the refined candidate seed search radius are shown in Fig. 6c) and d), respectively. The CPD approach provided decreased mean TREs compared to the spring approach for search radii <4 mm, with a minimum value with a search radius of 3 mm. Similarly, the CPD approach provided decreased maximum

465 TREs for search radii <6 mm, with a minimum value with a search radius of 3 mm. Both
466 deformable registration approaches demonstrated increases in TRE with search radii >3
467 mm. A refined candidate seed search radius of 3 mm was selected as the default value.

IV.   Discussion

469 We have presented an algorithm for deformable registration of X-ray images and MRI for
470 PPB post-implant dosimetry. This algorithm enables a clinical workflow where soft tissue
471 contouring can by performed using MRI, and dose can be calculated in the MRI coordinate
472 system without the need for CT. By saving seed locations in DICOM-RT format, it would
473 be possible to use commercially available treatment planning systems for dose calculation.
474 Replacing the CT scan with three projection X-rays for seed localization reduces the effective
475 imaging dose by a factor of $\sim$10,[47] and reduces clinical resource requirements. The TRE
476 distributions following the deformable-CPD registration approach resulted in mean$\pm$SD error
477 in prostate D90 of 2.3$\pm$1.9%. This dosimetric error resulting from the TRE distribution
478 with mean of 1.76 mm coincide with the simulation results of Su et al., which indicated
479 that normally-distributed seed localization errors with 2 mm standard deviation lead to
480 prostate D90 errors within 5%.[48] Prostate D90 has previously been correlated with clinical
481 outcomes,[49] and an uncertainty in D90 of 5% has been suggested to be clinically reasonable
482 in the context of other sources of uncertainty, such as contouring.[50]

483   In this study, we compared two general approaches for deformable point cloud registra-
484 tion,[27] and found that the CPD approach resulted in decreased TRE and computation time
485 when compared to the spring model-based gradient descent approach. To our knowledge,
486 the spring model approach is the only other algorithm previously investigated for this ap-
487 plication.[34] The comparison showed that the CPD approach led to a statistically significant
488 decrease in the maximum TREs. The results of the sensitivity analysis suggest that spring
489 model-based regularization may limit seed translations to a greater degree than the CPD
490 approach, where the spring model provides smaller TREs than the CPD approach for refined
491 candidate search radii >4 mm. Decreasing the coefficient of the regularization term of the
492 spring model cost function may lead to small improvements in accuracy; however, the CPD
493 algorithm led to improved registration accuracy for the data in this study. Furthermore, the
494 accuracy of both deformable registration approaches appeared to be limited by the quality

---

Last edited $June 17, 2019$

of the candidate seeds identified from MRI, which is limited by image quality. The results of the sensitivity analysis suggest optimal parameters for candidate seed localization and refinement using clinical T2 weighted MRI using either deformable registration approach.

A limitation of the images analyzed in this study was the spatial resolution of the clinical T2 weighted MRI, which had mean voxel dimensions of $0.8 \times 0.8 \times 3.0$ mm^3. The rigid and affine registration steps led to TREs with smaller out-of-plane than in-plane components, potentially attributed to the 0.4 mm superior-inferior spatial resolution of the X-rays used for initial seed reconstruction. Deformable registration using the spring-model or CPD approach led to TREs with smaller in-plane than out-of-plane components, suggesting that improved deformable registration accuracy can be achieved through improved MRI spatial resolution. We did not directly evaluate the application of this algorithm to MR images acquired with different hardware or pulse sequences; however, the MRI pre-processing step involved signal intensity normalization within the prostate to limit sensitivity to changes in signal gain. Furthermore, we did not directly evaluate the application of this algorithm to different seed models; however, we expect that seed models leading to local hypo-intensities can be identified in the pre-processing step and used for deformable registration.

Limited spatial resolution of the CT likely also contributed to the measured TREs through non-zero target localization error from both the manual identification of seeds on CT and registration of the CT to MRI[51]. Inter-observer variability in CT-based seed localization has been shown to be 1.1 mm.[12] The CT and MRI registration accuracy may also have been influenced by the landmarks chosen for alignment, the CT and MRI acquisition parameters, or changes in patient position, bladder and rectum filling between the CT and MRI scans. Registration errors between CT and MRI would lead to systematic increases in measured TRE.

The image acquisition timeline used in this study was selected to provide test images (X-ray and MRI) and a reasonable ground truth (CT) for deformable registration while remaining clinically feasible. The timeline began with X-rays acquired immediately following the PPB implant followed by CT and MRI acquired the next day. In this scenario, we expect prostate deformations to occur between X-ray imaging and CT/MRI, thereby producing images that test the ability for the algorithm to perform deformable registration between X-rays and MRI *in vivo*. A limitation of this approach is the short time elapsing between CT and

IV.   DISCUSSION

526 MRI, during which further deformations may take place that would increase the measured
527 TREs. We specifically selected patient cases for algorithm validation that displayed little
528 or no visible deformation between CT and MRI to mitigate this effect. Another limitation
529 of this timeline is that the changes in seed position observed between X-rays and MRI are
530 likely larger than those that would be expected clinically, where we expect X-rays and MRI
531 to be acquired on the same day, similar to the CT/MRI approach. A portion of the 1.3% of
532 seeds with TREs >5 mm may have been caused by seed migration taking place in this one
533 day interval.

534   In this study, we considered seeds implanted within the prostate and outside of the
535 prostate within 1 cm of the prostate periphery, which commonly arise in peripherally loaded
536 treatment plans. Seeds at the prostate periphery, particularly within the seminal vesicles,
537 base, and apex may migrate following insertion.[52] Visual inspection of the seeds with TREs
538 >5 mm suggest that most of the apparent registration errors occurred in these regions prone
539 to seed migration. For clinical post-implant dosimetry, X-rays used for seed reconstruction
540 will typically be acquired on the same day as the MRI to mitigate potential seed migration
541 and reduce the maximum TREs, similar to the CT/MRI approach. The deformable regis-
542 tration algorithm is currently limited to account for local deformations ≤3 mm. Based on
543 the results from this study, a 3 mm search neighborhood is sufficient to model most local
544 prostate deformations while avoiding errors introduced by nearby seeds.

545   Finally, the X-ray and MRI-based post-implant dosimetry approach proposed in this
546 study depends critically on the geometric accuracy of the MRI. This type of geometric
547 error could lead to dosimetric errors when X-ray-based seeds are deformably registered to
548 the MRI. The MR images analyzed in this study were acquired using the MRI simulator
549 in our radiation oncology department, which corrects for geometric distortions using an
550 algorithm available in the Siemens console workstation (Syngo).[53,54] The MRI simulator
551 also undergoes daily and monthly quality assurance using a phantom designed to detect
552 geometric distortions.

V. Conclusions

We have proposed novel X-ray and MRI registration methods for PPB post-implant dosimetry. The proposed method requires only three X-rays acquired using a mobile C-arm imaging system for seed localization in the MRI coordinate system, potentially enabling reliable post-implant dosimetry without the need for CT. The total combined execution time of the X-ray based seed reconstruction and deformable registration is 36.1 s. The algorithm accuracy and computation time is sufficient for clinical PPB post-implant dosimetry.

Appendix

The derivation of the spring model-based cost function is described as follows, extended from the method proposed by Park et al.[34] First, we define an external energy term $U_{E,i}$ for each seed $\vec{s}_i$ in the moving point set as

$$U_{E,i} = D(\vec{s}_i + \Delta\vec{s}_i) \tag{7}$$

where $D(\vec{p})$ is the distance from $\vec{p}$ to the nearest candidate seed location as defined in Eq. 2 and $\Delta\vec{s}_i$ is a set of local $[\Delta x_i, \Delta y_i, \Delta z_i]$ displacement components. We then define an internal energy term $U_{I,i}$ based on a non-linear spring model between adjacent seeds. Hooke's law states that the restoring force F exerted by a spring displaced by distance ΔL is given by $F = k\Delta L$ where k is a spring constant. In an ideal spring, k is inversely proportional to the original spring length L. To allow local deformations while preventing large translations that may change seed cloud topology, we define a non-linear spring constant for a pair of seeds $\vec{s}_i$ and $\vec{s}_j$ as

$$k_{i,j} = \frac{\lambda}{L_{i,j}^2} \tag{8}$$

where λ is a constant defining the spring stiffness and

$$L_{i,j} = \|\vec{s}_i - \vec{s}_j\| \tag{9}$$

V. CONCLUSIONS

576 The potential energy $U_{I,i,j}$ associated with a displacement $\Delta L_{i,j}$ is then

577
$$U_{I,i,j} = \frac{\lambda}{2}\left(\frac{\Delta L_{i,j}}{L_{i,j}}\right)^2 \tag{10}$$

578 The term $\Delta L_{i,j}$ is approximated for two seeds $\vec{s}_i$ and $\vec{s}_j$ displaced by vectors $\Delta\vec{s}_i$ and $\Delta\vec{s}_j$,
579 as

580
$$\Delta L_{i,j} = \|(\vec{s}_i + \Delta\vec{s}_i) - (\vec{s}_j + \Delta\vec{s}_j)\| - \|\vec{s}_i - \vec{s}_j\|$$
$$\approx \|\Delta\vec{s}_i - \Delta\vec{s}_j\| \tag{11}$$

581 The internal energy for seed $\vec{s}_i$ surrounded by Q neighboring seeds is then

582
$$U_{I,i} = \frac{\lambda}{2}\sum_{j=1}^{Q}\left(\frac{\|\Delta\vec{s}_i - \Delta\vec{s}_{P(i,j)}\|}{\|\vec{s}_i - \vec{s}_{P(i,j)}\|}\right)^2 \tag{12}$$

583 where P is a two-dimensional array of indices in which element $P(i,j)$ is the index of the
584 j^{th}-nearest neighbor to $\vec{s}_i$. The spring model cost function is then defined according to Eq.
585 4 where the external and internal energy terms are defined for the set of N seeds as

586
$$U_E(\nu_{spring}) = \sum_{i=1}^{N} D(\vec{s}_i + \Delta\vec{s}_i) \tag{13}$$

587
$$\frac{\lambda}{2}U_I(\nu_{spring}) = \frac{\lambda}{2}\sum_{i=1}^{N}\sum_{j=1}^{Q}\left(\frac{\|\Delta\vec{s}_i - \Delta\vec{s}_{P(i,j)}\|}{\|\vec{s}_i - \vec{s}_{P(i,j)}\|}\right)^2 \tag{14}$$

588 where λ can be interpreted as the spring stiffness or degree of regularization, and ν_{spring} is
589 the set of local displacements $\{\Delta\vec{s}_1, \Delta\vec{s}_2... \Delta\vec{s}_N\}$. Values of Q and λ of 5 and 40 were used in
590 this study. P was populated prior to optimization using a Kd-tree nearest neighbors search
591 algorithm.[43] Using the spring model energy terms, Eq. 4 was minimized using gradient
592 descent optimization based on the partial derivatives

593
$$\frac{\partial f(\nu_{spring})}{\partial\Delta u_i} = \frac{\nabla D(\vec{s}_i + \Delta\vec{s}_i)_u}{D(\vec{s}_i + \Delta\vec{s}_i)} + \lambda\sum_{j=1}^{M}\frac{\Delta u_i - \Delta u_{P(i,j)}}{\|\vec{s}_i - \vec{s}_{P(i,j)}\|^2} \tag{15}$$

594 where u is x, y, or z.

Last edited $June 17, 2019$

Acknowledgment

V. CONCLUSIONS

References

[1] N. Mottet et al., EAU-ESTRO-SIOG Guidelines on Prostate Cancer. Part 1: Screening, Diagnosis, and Local Treatment with Curative Intent, European Urology **71**, 618–629 (2017).

[2] W. J. Morris, S. Tyldesley, S. Rodda, R. Halperin, H. Pai, M. McKenzie, G. Duncan, G. Morton, J. Hamm, and N. Murray, Androgen Suppression Combined with Elective Nodal and Dose Escalated Radiation Therapy (the ASCENDE-RT Trial): An Analysis of Survival Endpoints for a Randomized Trial Comparing a Low-Dose-Rate Brachytherapy Boost to a Dose-Escalated External Beam Boost, International Journal of Radiation Oncology Biology Physics **98**, 275–285 (2017).

[3] J. Lee, O. Y. Mian, Y. Le, H. J. Bae, E. C. Burdette, T. L. DeWeese, J. L. Prince, and D. Y. Song, Intraoperative Registered Ultrasound and Fluoroscopy (iRUF) for dose calculation during prostate brachytherapy: Improved accuracy compared to standard ultrasound-based dosimetry, Radiotherapy and Oncology **124**, 61–67 (2017).

[4] J. Lee, R. F. Hobbs, M. Zahurak, S. K. Ng, Z. Zhang, E. C. Burdette, T. L. DeWeese, and D. Y. Song, Phase II study of intraoperative dosimetry for prostate brachytherapy using registered ultrasound and fluoroscopy, Brachytherapy **17**, 858–865 (2018).

[5] B. J. Davis, E. M. Horwitz, W. R. Lee, J. M. Crook, R. G. Stock, G. S. Merrick, W. M. Butler, P. D. Grimm, N. N. Stone, L. Potters, A. L. Zietman, and M. J. Zelefsky, American Brachytherapy Society consensus guidelines for transrectal ultrasound-guided permanent prostate brachytherapy, Brachytherapy **11**, 6–19 (2012).

[6] D. Taussky, L. Austen, A. Toi, I. Yeung, T. Williams, S. Pearson, M. McLean, G. Pond, and J. Crook, Sequential evaluation of prostate edema after permanent seed prostate brachytherapy using CT-MRI fusion, International Journal of Radiation Oncology Biology Physics **62**, 974–980 (2005).

[7] S. Nag, W. Bice, K. DeWyngaert, B. Prestidge, R. Stock, and Y. Yu, The American Brachytherapy Society recommendations for permanent prostate brachytherapy postimplant dosimetric analysis, International Journal of Radiation Oncology Biology Physics **46**, 221–230 (2000).

Last edited $June 17, 2019$

[628] 8 R. Nath, W. S. Bice, W. M. Butler, Z. Chen, A. S. Meigooni, V. Narayana, M. J. Rivard,
[629]   and Y. Yu, AAPM recommendations on dose prescription and reporting methods for
[630]   permanent interstitial brachytherapy for prostate cancer: report of Task Group 137.,
[631]   Medical Physics **36**, 5310–5322 (2009).

[632] 9 S. A. Rosenthal, N. H. J. Bittner, D. C. Beyer, D. J. Demanes, B. J. Goldsmith, E. M.
[633]   Horwitz, G. S. Ibbott, W. R. Lee, S. Nag, W. W. Suh, and L. Potters, American
[634]   society for radiation oncology (ASTRO) and American College of Radiology (ACR)
[635]   practice guideline for the transperineal permanent brachytherapy of prostate cancer,
[636]   International Journal of Radiation Oncology Biology Physics **79**, 335–341 (2011).

[637] 10 K. J. Gregory, J. E. Pattison, and G. Bibbo, Measurement uncertainty analysis of low-
[638]   dose-rate prostate seed brachytherapy: post-implant dosimetry, Australasian Physical
[639]   and Engineering Sciences in Medicine **38**, 71–81 (2015).

[640] 11 A. Polo, F. Cattani, A. Vavassori, D. Origgi, G. Villa, H. Marsiglia, M. Bellomi, G. Tosi,
[641]   O. De Cobelli, and R. Orecchia, MR and CT image fusion for postimplant analysis in
[642]   permanent prostate seed implants, International Journal of Radiation Oncology Biology
[643]   Physics **60**, 1572–1579 (2004).

[644] 12 M. De Brabandere, B. Al-Qaisieh, L. De Wever, K. Haustermans, C. Kirisits, M. A.
[645]   Moerland, R. Oyen, A. Rijnders, F. Van den Heuvel, and F. A. Siebert, CT- and
[646]   MRI-based seed localization in postimplant evaluation after prostate brachytherapy,
[647]   Brachytherapy **12**, 580–588 (2013).

[648] 13 H. Kunogi, H. Hojo, Y. Wakumoto, A. I. Saito, S. Ishikura, Y. Yamashiro, R. Kuwatsuru,
[649]   and K. Sasai, A new two-step accurate CT-MRI fusion technique for post-implant
[650]   prostate cancer, Journal of Contemporary Brachytherapy **7**, 117–121 (2015).

[651] 14 O. Tanaka, S. Hayashi, M. Matsuo, K. Sakurai, M. Nakano, S. Maeda, K. Kajita,
[652]   T. Deguchi, and H. Hoshi, Comparison of MRI-based and CT/MRI fusion-based postim-
[653]   plant dosimetric analysis of prostate brachytherapy, International Journal of Radiation
[654]   Oncology Biology Physics **66**, 597–602 (2006).

[655] 15 F. Zijlstra, M. A. Moerland, J. R. N. Van Der Voort Van Zyp, J. L. Noteboom, M. A.

Viergever, and P. R. Seevinck, Challenges in MR-only seed localization for postimplant dosimetry in permanent prostate brachytherapy, Medical Physics **44**, 5051–5060 (2017).

[16] T. Y. Lim, R. J. Kudchadker, J. Wang, R. J. Stafford, C. Maclellan, A. Rao, G. S. Ibbott, and S. J. Frank, Effect of pulse sequence parameter selection on signal strength in positive-contrast MRI markers for MRI-based prostate postimplant assessment, Medical Physics **43**, 4312–4322 (2016).

[17] J. W. Sanders, H. Song, S. J. Frank, T. Bathala, A. M. Venkatesan, M. Anscher, C. Tang, T. L. Bruno, W. Wei, and J. Ma, Parallel imaging compressed sensing for accelerated imaging and improved signal-to-noise ratio in MRI-based postimplant dosimetry of prostate brachytherapy, Brachytherapy **17**, 816–824 (2018).

[18] N. Kuo, J. Lee, C. Tempany, M. Stuber, and J. Prince, MRI-based prostate brachytherapy seed localization, in *IEEE International Symposium on Biomedical Imaging*, pages 1397–1400, 2010.

[19] Y. Dong, Z. Chang, G. Xie, G. Whitehead, and J. X. Ji, Susceptibility-based positive contrast MRI of brachytherapy seeds, Magnetic Resonance in Medicine **74**, 716–726 (2015).

[20] R. Nosrati, A. Soliman, H. Safigholi, M. Hashemi, M. Wronski, G. Morton, A. Pejović-Milić, G. Stanisz, and W. Y. Song, MRI-based automated detection of implanted low dose rate (LDR) brachytherapy seeds using quantitative susceptibility mapping (QSM) and unsupervised machine learning (ML), Radiotherapy and Oncology - In Press (2018).

[21] R. Nosrati, M. Wronski, A. Ravi, H. Safigholi, A. Pejović-Milić, G. Stanisz, and G. Morton, MRI-Based Post-Implant Dosimetry of Prostate Brachytherapy Seeds, in *Brachytherapy*, volume 17, pages S73–S74, 2018.

[22] P. Acher, K. Rhode, S. Morris, A. Gaya, M. Miquel, R. Popert, I. Tham, J. Nichol, K. McLeish, C. Deehan, P. Dasgupta, R. Beaney, and S. F. Keevil, Comparison of Combined X-Ray Radiography and Magnetic Resonance (XMR) Imaging-Versus Computed Tomography-Based Dosimetry for the Evaluation of Permanent Prostate Brachytherapy Implants, International Journal of Radiation Oncology Biology Physics **71**, 1518–1525 (2008).

Last edited $June 17, 2019$

[23] P. Acher, S. Puttagunta, K. Rhode, S. Morris, J. Kinsella, A. Gaya, P. Dasgupta, C. Deehan, R. Beaney, R. Popert, and S. Keevil, An analysis of intraoperative versus postoperative dosimetry with CT, CT-MRI fusion and XMR for the evaluation of permanent prostate brachytherapy implants, Radiotherapy and Oncology **96**, 166–171 (2010).

[24] J. Lee, N. Kuo, A. Deguet, E. Dehghan, D. Y. Song, E. C. Burdette, and J. L. Prince, Intraoperative 3D reconstruction of prostate brachytherapy implants with automatic pose correction, Physics in Medicine and Biology **56**, 5011–5027 (2011).

[25] E. Dehghan, J. Lee, P. Fallavollita, N. Kuo, A. Deguet, Y. Le, E. Clif Burdette, D. Y. Song, J. L. Prince, and G. Fichtinger, Ultrasound-fluoroscopy registration for prostate brachytherapy dosimetry, Medical Image Analysis **16**, 1347–1358 (2012).

[26] N. Kuo, E. Dehghan, A. Deguet, O. Y. Mian, Y. Le, E. C. Burdette, G. Fichtinger, J. L. Prince, D. Y. Song, and J. Lee, An image-guidance system for dynamic dose calculation in prostate brachytherapy using ultrasound and fluoroscopy, Medical Physics **41**, 91712-1–13 (2014).

[27] G. K. L. Tam, Z. Q. Cheng, Y. K. Lai, F. C. Langbein, Y. Liu, D. Marshall, R. R. Martin, X. F. Sun, and P. L. Rosin, Registration of 3D point clouds and meshes: A survey from rigid to Nonrigid, IEEE Transactions on Visualization and Computer Graphics **19**, 1199–1217 (2013).

[28] B. J. Brown and S. Rusinkiewicz, Global non-rigid alignment of 3-D scans, in *ACM SIGGRAPH 2007 papers on - SIGGRAPH '07*, page 21, 2007.

[29] A. Myronenko and X. Song, Point set registration: Coherent point drifts, IEEE Transactions on Pattern Analysis and Machine Intelligence **32**, 2262–2275 (2010).

[30] A. L. Yuille and N. M. Grzywacz, A mathematical analysis of the motion coherence theory, International Journal of Computer Vision **3**, 155–175 (1989).

[31] P. Zhang, Y. Qiao, S. Wang, J. Yang, and Y. Zhu, A robust coherent point drift approach based on rotation invariant shape context, Neurocomputing **219**, 455–473 (2017).

[32] D. Aiger, N. J. Mitra, and D. Cohen-Or, 4-points congruent sets for robust pairwise surface registration, in *ACM SIGGRAPH 2008 papers on - SIGGRAPH '08*, page 1, 2008.

[714] [33] J. Lee, C. Labat, A. K. Jain, D. Y. Song, E. C. Burdette, G. Fichtinger, and J. L.
[715]   Prince, REDMAPS: Reduced-dimensionality matching for prostate brachytherapy seed
[716]   reconstruction, IEEE Transactions on Medical Imaging **30**, 38–51 (2011).

[717] [34] S. Park, D. Y. Song, and J. Lee, Deformable registration of X-ray to MRI for post-
[718]   implant dosimetry in prostate brachytherapy, Progress in Biomedical Optics and Imag-
[719]   ing - Proceedings of SPIE **9786** (2016).

[720] [35] M. Styner, C. Brechbuler, G. Szekely, and G. Gerig, Parametric estimate of intensity
[721]   inhomogeneities applied to MRI, IEEE Transactions on Medical Imaging **19**, 153–165
[722]   (2000).

[723] [36] Y. Chen and G. Medioni, Object modeling by registration of multiple range images, in
[724]   *IEEE International Conference on Robotics and Automation*, pages 2724–2729, Elsevier,
[725]   1991.

[726] [37] S. Umeyama, Least-Squares Estimation of Transformation Parameters Between Two
[727]   Point Patterns, IEEE Transactions on Pattern Analysis and Machine Intelligence **13**,
[728]   376–380 (1991).

[729] [38] M. J. Rivard, B. M. Coursey, L. a. DeWerd, W. F. Hanson, M. S. Huq, G. S. Ibbott,
[730]   M. G. Mitch, R. Nath, and J. F. Williamson, Update of AAPM Task Group No. 43
[731]   Report: A revised AAPM protocol for brachytherapy dose calculations., Medical physics
[732]   **31**, 633–674 (2004).

[733] [39] L. Beaulieu, Å. Carlsson Tedgren, J. F. Carrier, S. D. Davis, F. Mourtada, M. J. Rivard,
[734]   R. M. Thomson, F. Verhaegen, T. A. Wareing, and J. F. Williamson, Report of the Task
[735]   Group 186 on model-based dose calculation methods in brachytherapy beyond the TG-
[736]   43 formalism: Current status and recommendations for clinical implementation, Medical
[737]   Physics **39**, 6208–6236 (2012).

[738] [40] N. Kuo, A. Deguet, D. Y. Song, E. C. Burdette, J. L. Prince, and J. Lee, Auto-
[739]   matic segmentation of radiographic fiducial and seeds from X-ray images in prostate
[740]   brachytherapy, Medical Engineering and Physics **34**, 64–77 (2012).

Last edited $June 17, 2019$

[41] K. Wachowicz, S. D. Thomas, and B. G. Fallone, Characterization of the susceptibility artifact around a prostate brachytherapy seed in MRI, Medical Physics **33**, 4459–4467 (2006).

[42] P. E. Danielsson, Euclidean distance mapping, Computer Graphics and Image Processing **14**, 227–248 (1980).

[43] M. Muja and D. G. Lowe, Fast approximate nearest neighbors with automatic algorithm configuration, in *International Conference on Computer Vision Theory and Applications*, 2009.

[44] R. H. Byrd, P. Lu, J. Nocedal, and C. Zhu, A limited memory algorithm for bound constrained optimization, SIAM Journal on Scientific and Statistical Computing **16**, 1190–1208 (1995).

[45] R. B. Rusu and S. Cousins, 3D is here: Point Cloud Library (PCL), in *IEEE International Conference on Robotics and Automation (ICRA)*, 2011.

[46] C. Pinter, A. Lasso, A. Wang, D. Jaffray, and G. Fichtinger, SlicerRT: radiation therapy research toolkit for 3D Slicer, Medical physics **39**, 6332–6338 (2012).

[47] M. J. Murphy, J. Balter, S. Balter, J. A. BenComo, I. J. Das, S. B. Jiang, C.-M. Ma, G. H. Olivera, R. F. Rodebaugh, K. J. Ruchala, H. Shirato, and F.-F. Yin, The management of imaging dose during image-guided radiotherapy: Report of the AAPM Task Group 75, Medical Physics **34**, 4041–4063 (2007).

[48] Y. Su, B. J. Davis, K. M. Furutani, M. G. Herman, and R. A. Robb, Dosimetry accuracy as a function of seed localization uncertainty in permanent prostate brachytherapy: Increased seed number correlates with less variability in prostate dosimetry, Physics in Medicine and Biology **52**, 3105–3119 (2007).

[49] L. Potters, C. Morgensteern, E. Calugaru, P. Fearn, A. Jassal, J. Presser, and E. Mullen, 12-year outcomes following permanent prostate brachytherapy in patients with clinically localized prostate cancer, The Journal of Urology **173**, 1562–1566 (2005).

[50] P. E. Lindsay, J. Van Dyk, and J. J. Battista, A systematic study of imaging uncertainties and their impact on 125I prostate brachytherapy dose evaluation., Medical physics **30**, 1897–1908 (2003).

51   J. M. Fitzpatrick and J. B. West, The Distribution of Target Registration Error in Rigid-Body Point-Based Registration, IEEE Transactions on Medical Imaging **20**, 917–927 (2001).

52   M. Nakano, A. Yorozu, S. Saito, A. Sugawara, S. Maruo, S. Kojima, T. Kikuchi, M. Fukushima, T. Dokiya, and H. Yamanaka, Seed migration after transperineal interstitial prostate brachytherapy by using loose seeds: Japanese prostate cancer outcome study of permanent iodine-125 seed implantation (J-POPS) multi-institutional cohort study, Radiation Oncology **10**, 228–240 (2015).

53   S. J. Doran, L. Charles-Edwards, S. A. Reinsberg, and M. O. Leach, A complete distortion correction for MR images: I. Gradient warp correction, Physics in Medicine and Biology **50**, 1343–1361 (2005).

54   C. P. Karger, A. Höss, R. Bendl, V. Canda, and L. Schad, Accuracy of device-specific 2D and 3D image distortion correction algorithms for magnetic resonance imaging of the head provided by a manufacturer, Physics in Medicine and Biology **51**, N253–261 (2006).

Last edited $June 17, 2019$

Figure Captions

Figure 1. Flow chart outlining the proposed deformable X-ray and MRI registration algorithm.

Figure 2. Example MR images with registered X-ray-based seed locations from two patients.

Figure 3. Histograms of TREs following each registration step for 1774 seeds. Mean values are indicated by the dashed lines.

Figure 4. Boxplots of TREs for each step of the registration algorithm for each patient. Center-lines indicate medians, boxes indicate inter-quartile range, and dots indicate TREs for each seed.

Figure 5. a) Boxplots of of the prostate D90 error relative to the CT and MRI-based post-implant dosimetry approach. Center-lines indicate medians, boxes indicate inter-quartile range, and dots indicate the error for each patient. b-g) Example MRI and corresponding dose distributions in the MRI coordinate system.

Figure 6. a) Plot of the number of candidate seeds locations identified versus the constraint on maximum number of candidate seeds, both normalized to the number of seeds implanted. b) Mean rigid TRE versus the constraint on the maximum number of candidate seeds. c) Mean deformable TRE versus the refined candidate seed search radius. d) Maximum deformable TRE versus the refined candidate seed search radius. In all plots, dots represent the mean value across patients and error bars represent standard error.

Tables

Table 1: Mean±SD TRE metrics across patients (mm).

TRE Component	Method	Mean	SD	Max.
Total	Rigid	2.23±0.52	1.04±0.27	5.86±1.58
	Affine	1.99±0.49	1.00±0.23	5.59±1.32
	Deformable-Spring	1.81±0.48	0.99±0.24	5.37±1.25
	Deformable-CPD	1.76±0.43	0.93±0.23	5.07±1.38
In-plane	Rigid	1.56±0.48	0.90±0.25	5.14±1.57
	Affine	1.34±0.39	0.84±0.24	4.82±1.53
	Deformable-Spring	1.14±0.34	0.79±0.24	4.57±1.46
	Deformable-CPD	1.09±0.30	0.75±0.23	4.37±1.39
Out-of-plane	Rigid	1.33±0.36	0.95±0.24	4.44±1.61
	Affine	1.24±0.36	0.91±0.19	4.16±1.22
	Deformable-Spring	1.21±0.35	0.91±0.19	4.18±1.22
	Deformable-CPD	1.19±0.31	0.87±0.19	3.97±1.26

Last edited $June 17, 2019$

Figures

Figure 1: Flow chart outlining the proposed deformable X-ray and MRI registration algorithm.
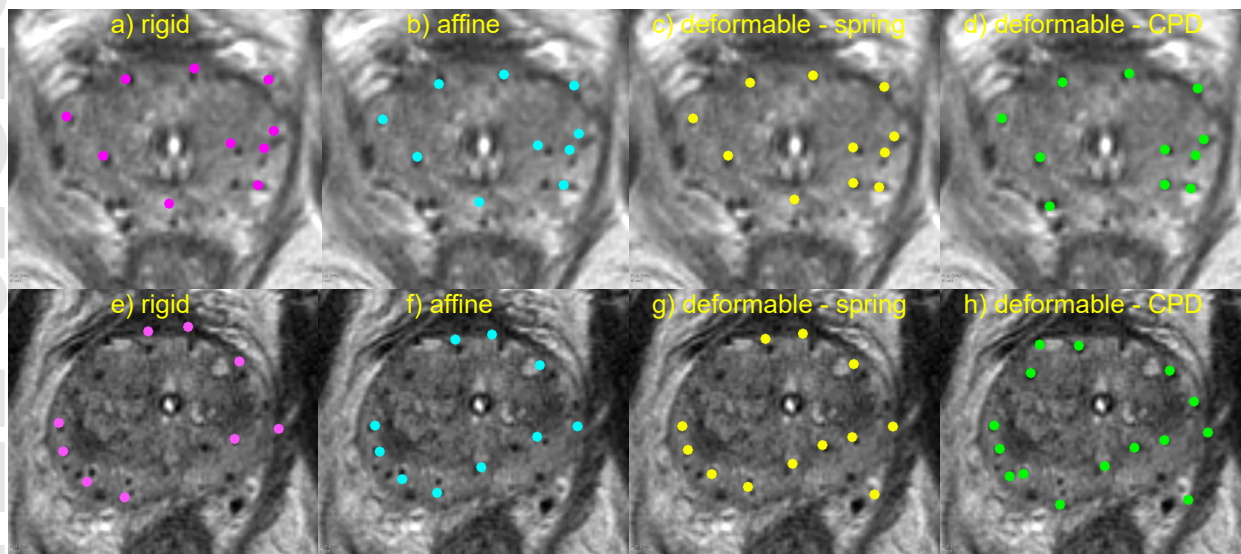
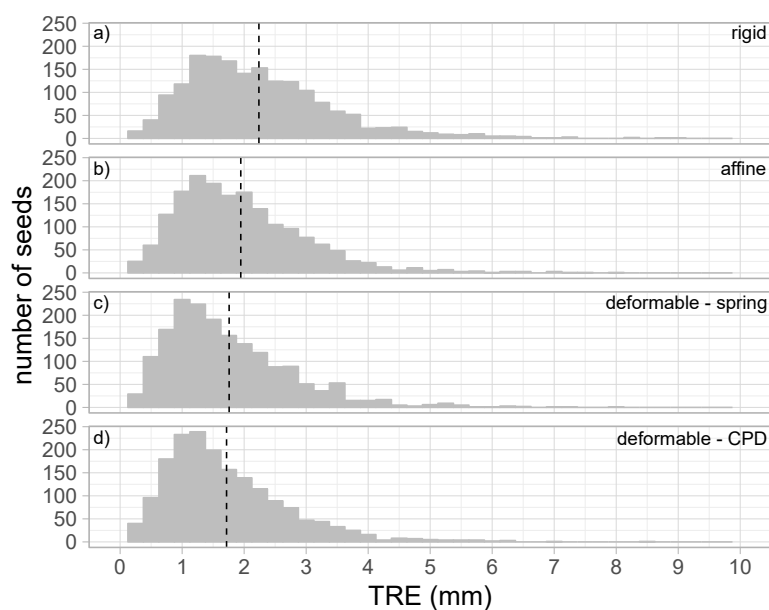Figure 2: Example MR images with registered X-ray-based seed locations from two patients.

Figure 3: Histograms of TREs following each registration step for 1774 seeds. Mean values are indicated by the dashed lines.
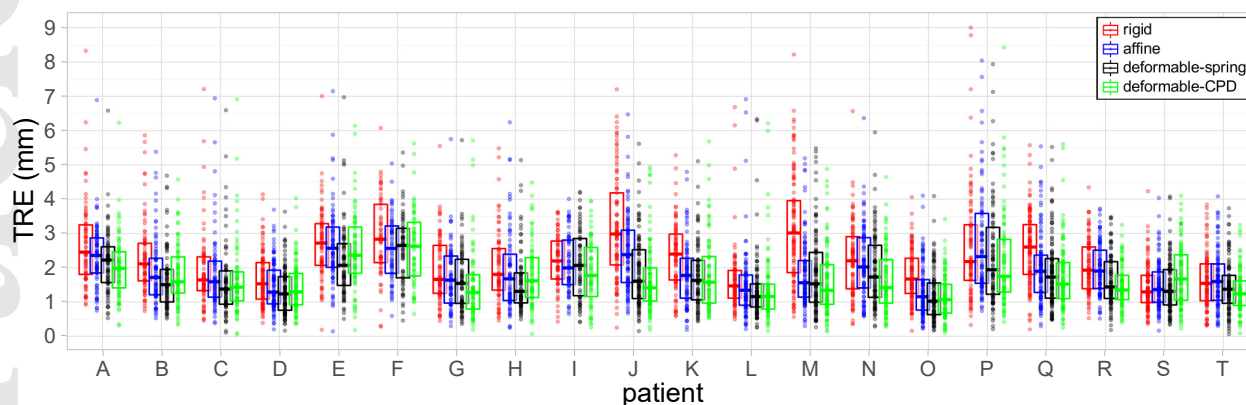
Figure 4: Boxplots of TREs for each step of the registration algorithm for each patient. Center-lines indicate medians, boxes indicate inter-quartile range, and dots indicate TREs for each seed.
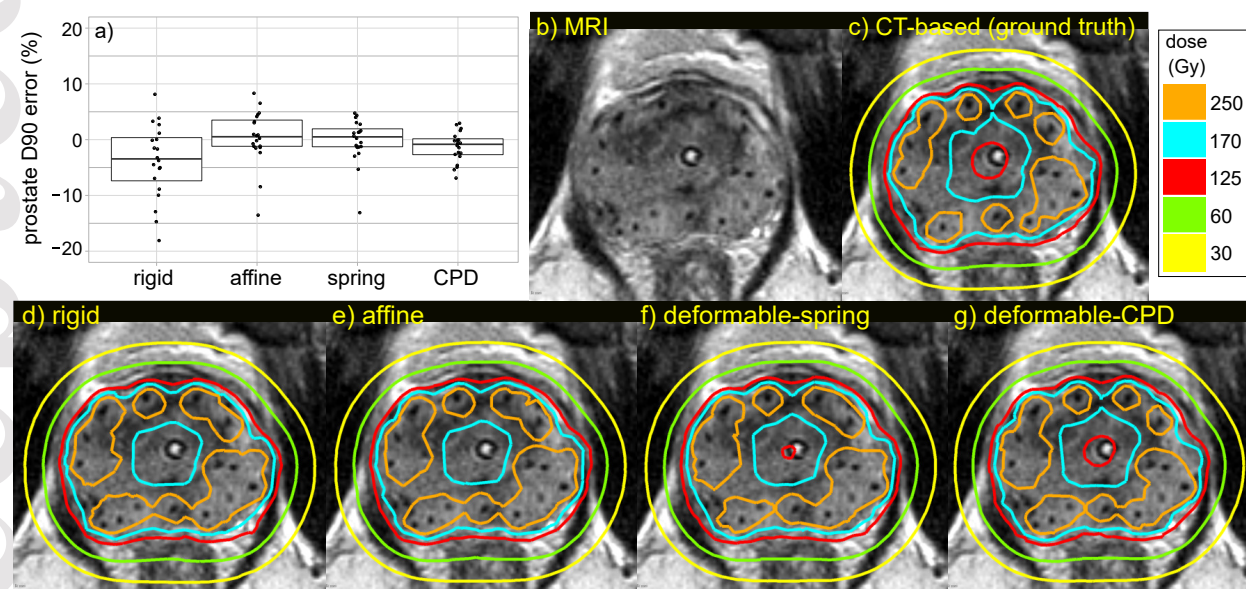

Figure 5: a) Boxplots of of the prostate D90 error relative to the CT and MRI-based post-implant dosimetry approach. Center-lines indicate medians, boxes indicate inter-quartile range, and dots indicate the error for each patient. b-g) Example MRI and corresponding dose distributions in the MRI coordinate system.
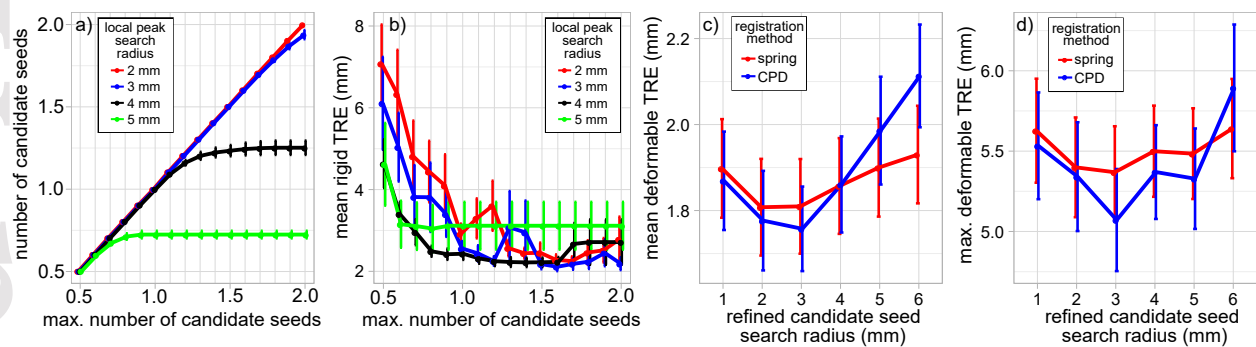
Figure 6: a) Plot of the number of candidate seeds locations identified versus the constraint on maximum number of candidate seeds, both normalized to the number of seeds implanted. b) Mean rigid TRE versus the constraint on the maximum number of candidate seeds. c) Mean deformable TRE versus the refined candidate seed search radius. d) Maximum deformable TRE versus the refined candidate seed search radius. In all plots, dots represent the mean value across patients and error bars represent standard error.